Hierarchical Placement Strategy for Grid-Forming Energy Storage Considering Multi-Timescale Stability Enhancement

Yushan Liu, Junru Chen, *Member, IEEE*, Muyang Liu, *Member, IEEE* and Federico Milano, *Fellow, IEEE*

***Abstract*-- This paper proposes a hierarchical site selection framework of grid-forming energy storage (GFM-ESS) devices. This framework enhances stability of both the device itself and the power system across multi-timescales with respect to static, dynamic, and transient stability layouts. Specifically, the first layout optimizes static voltage stability margin and system losses. The second layout evaluates small-signal stability based on the generalized short-circuit ratio (gSCR). Finally, the third layout maximizes the GFM-ESS supporting performance in response to the system dynamics. A case study based on Western China serves to validate the effectiveness of the proposed GFM-ESS site selection strategy and to prove its scalability for large real-world power systems.**

***Index Terms*-- Energy storage, frequency response, grid-forming, planning, power system stability, voltage fluctuations.**

I. Introduction

Power systems are migrating to higher penetration of the inverter-based resources (IBRs). Most of the present IBRs are working in grid-following (GFL) mode with barely any inertia and damping effect [1][1]. The replacement of the synchronous generators (SGs) with these IBRs increases the risk of frequency and voltage instability [2], [3][2][3]. In this context, the grid-forming energy storage system (GFM-ESS) has been proposed to maintain the stability of the power system [4], [5]. This device mimics the inertia and damping characteristics of SG, provides voltage and frequency support to the grid and shows superior adaptability to weak grids. Therefore, GFM-ESS is regarded as an effective mean to address the series of challenges brought by the high penetration of IBRs, and has already been applied in power systems, e.g. the 300 MW/450 MWh Victorian GFM-ESS project in Moorabool, Victoria, and the 200 MW/400 MWh GFM-ESS in Blyth, South Australia [6][6]. In the above demonstration projects, the site of the GFM-ESS was arbitrarily selected without considering its advanced supporting effect on the grid. This may result in under-utilization of the device's grid-forming capability, thereby reducing cost-effectiveness.

GFM-ESSs offer not only energy shifting, but also active voltage/frequency support and superior weak-grid adaptability. These features should be explicitly considered in the early planning stage and siting strategies should be aligned with the supporting requirements of high-penetration IBR systems. However, most existing research focuses on the GFM-ESS device itself, such as advanced control strategies and operational stability analysis [7]-[9]. As a result, how to define the optimal placement of GFM-ESS, particularly in terms of power system planning, is still an open question.

Compared with GFL-ESS, GFM-ESS has quicker reactions and presents higher power density in response to contingencies [10][10]. Regarding virtual inertia provision, GFM-ESS can effectively reduce the rate of change of frequency (RoCoF) and improve the frequency nadir during frequency disturbances [11], [12][2][3]. As for the voltage support, GFM-ESS can sustain its output voltage and actively provide reactive power according to its voltage difference to the grid [13]. Moreover, in weak power grids with very low short-circuit ratio (SCR), GFL-ESS are more prone to induce wide-band oscillations [14], while GFM-ESS can even enhance the system small-signal stability margin by actively introducing positive damping [15]. Therefore, the characteristics of GFM-ESS can meet the multi-timescale regulation requirements of high-penetration IBR systems from the timescale of milliseconds to minutes, meanwhile effectively adapting to weak grid scenarios [16][16]. Although the capital cost of GFM-ESS is much higher than that of GFL-ESS, GFM-ESS provides a greater capability in the power system support, which has the potential benefit of reducing the power system operational cost as a trade-off. Before widespread implementation of the GFM-ESS, it is crucial to determine the optimal site selection based on GFM characteristics, considering its contributions to both device-level and system-level stability. This paper aims at filling this gap and proposes a strategic approach for optimal GFM-ESS site selection.

Large-scale ESS station is normally co-located with a renewable power plant to facilitate the integration of renewable energy. Reference [17] proposes a cost-effective ESS siting

This work was supported in part by the Science and Technology Department of Xinjiang under Grant No. 2022A01004-1.

Yushan Liu is with the School of Electrical Engineering, Xinjiang University, Urumqi, 830047, China (e-mail: yushan_liu@stu.xju.edu.cn).

Junru Chen is with the Department of Electrical Engineering, Xinjiang University, Urumqi, 830047, China (corresponding author, e-mail: junru.chen@xju.edu.cn).

Muyang Liu is with the Department of Electrical Engineering, Xinjiang University, Urumqi, 830047, China (e-mail: muyang.liu@xju.edu.cn).

Federico Milano is with the School of Electrical and Electronic Engineering, University College Dublin, Dublin 4, Ireland (e-mail: federico.milano@ucd.ie).

strategy that minimizes both operational and investment costs while incorporating constraints to reduce renewable curtailment, but this method does not explore the potential benefits of the ESS's on the power system stability. Considering the frequency regulation capability of ESS, the siting model developed in [18] incorporates this characteristic to derive the optimal ESS placement under renewable energy fluctuations. In terms of system voltage regulation, [19][19] employs a Benders decomposition technique with multiple restarts to optimize the placement of static var compensators, aiming at maximizing the loading margin while accounting for voltage stability constraints. Leveraging on these results, voltage sensitivities and eigenvalue analysis have been considered in [20] to develop a stochastic planning model for ESS. A multi-objective approach for siting and sizing ESS to control frequency excursions and to alleviate line overloads during major disturbances is presented in [21][21]. In addition, some studies have considered the spatio-temporal distribution of ESS virtual inertia and optimized the allocation of IBRs for frequency support [22], [23]. These studies focus on medium- to long-term static indicators, such as peak shaving, frequency regulation, and energy shifting, which are appropriate for GFL-ESS. Research on the optimal site selection for GFM-ESS remains relatively limited.

Differ from GFL-ESS, GFM-ESS presents higher synchronization stability in weak grids or lower SCR systems and, most importantly, can help support the grid voltage and frequency, strengthening the system. The work in [24][24] is the first to consider the effect of GFM-ESS on the improvement of the small-signal stability and propose the optimal planning approach of GFM-ESS by increasing the smallest eigenvalue of the weighted and Kron-reduced Laplacian matrix of the grid. Based on this, an optimal planning approach with system strength constraints to address the GFM-ESS site selection problem has been proposed [25]. Small-signal stability and short-circuit current constraints can also be integrated into a MILP-based coordinated planning model involving synchronous condensers and GFM [26].

The studies mentioned above focus solely on the improvement of small-signal stability provided by GFM-ESS. In addition to the contribution of GFM-ESS to small-disturbance stability, its proper placement can also significantly enhance large-disturbance stability, such as 750 kV heavy line short-circuit or open-circuit, due to its voltage and frequency support capabilities. For power planning and operation, maximizing the beneficial impact of GFM-ESS devices is crucial for the Transmission System Operators (TSOs). Implementing GFM-ESS is an effective means to improve system stability and reduce operational costs. Thus, determining the optimal placement of GFM-ESS should comprehensively consider the stability requirements of the GFM-ESS itself and its contributions to power system operation and stability.

To fill this research gap on the GFM-ESS station planning in a large area, this paper proposes a hierarchical placement strategy from both the device- and system-levels across multiple timescales, including static and dynamic perspectives. The main innovations and specific contributions of this work are as follows.

1) A multi-stage siting framework is proposed to enhance stability across multiple time scales, by explicitly considering the contributions of GFM-ESS to system stability at different voltage levels.

2) A three-layout GFM-ESS site selection model with indices representing the effects of its implementation on static voltage stability, small-signal stability, and large-disturbance stability is proposed.

3) A real-world power system in Western China serves as a case study to illustrate the process of the proposed site selection strategy and to validate its effectiveness.

The remainder of the paper is organized as follows: Section II introduces the proposed GFM-ESS hierarchical siting framework. Section III details the three-layout siting model. Section IV illustrates the flowchart of the proposed siting strategy with feasible solution algorithms. Section V verifies the proposed strategy using a model of the Western China power system, while Section VI draws conclusions and outlines future work directions.

II. GFM-ESS Hierarchical Siting Framework

In large-scale power systems with thousands of nodes, pinpointing the optimal location for GFM-ESS installation to enhance stability across multiple time scales incurs a high computational cost, which attributes to the vast number of candidate sites, the complexity of multi-objective stability optimization, and the need to repeatedly run time-consuming power system simulations. To reduce the computational burden, this study proposes a GFM-ESS hierarchical siting framework that progressively narrows down potential sites considering multi-timescale stability enhancement to identify the specific optimal location, as illustrated in Fig. 1.

On the one hand, the GFM-ESS presents both the ESS and GFM features. It is fundamentally a storage which is used to balance the power supply and demand, and it can provide frequency and voltage support during transients. In the higher voltage-level power grid, e.g. 220 kV transmission system, the TSO puts more focus on the power dispatch in the normal operation of the system, while in the lower voltage-level power grid, e.g. 35 kV, the dynamic response of the devices and plants is more attended, especially during the grid fault.

On the other hand, the increase in the capacity of the GFL-devices/plant reduces the SCR of the connected node and increases the risk on the small-signal instability [27][27]. In contrast, GFM-ESS can enhance SCR and operate stably under low-SCR conditions [28][28]. Based on the above, the GFM-ESS hierarchical siting framework is proposed as follows:

The first layout study addresses the issue of 'Where to place the ESS among hundreds of 220kV grid nodes?'. This level focuses on the static voltage stability requirements of the system, fully considering the voltage regulation characteristics of ESS. By evaluating voltage static stability, reactive power compensation, and system losses, the first layout identifies the weaker nodes in the 220 kV transmission network to improve the system voltage stability.

The second layout study addresses the issue of 'Where should we place the GFM-ESS instead of the GFL-ESS?'. Considering that the weak grid adaptability of the GFM-ESS is more competitive than that of the GFL-ESS. Following the results from the first layout at a specific 220kV/110kV substation, this level aims to select the nodes where the GFM-ESS has higher small-signal stability than the GFL-ESS, to ensure the safe operation of ESS at the 110 kV voltage-level collector substation.

The third layout study addresses the issue of 'Which node is the best for the GFM-ESS with respect to grid frequency and voltage support across multiple time scales?'. Considering the transient support requirements of the system under large disturbances and based on the active support feature of GFM-ESS, this level aims to evaluate and identify the best synthetic effects on the grid dynamic frequency and voltage support. It specifies the renewable power plant at its 110kV /35kV station for the GFM-ESS replacement, ensuring that the power system gains maximum support from the same GFM-ESS investment.

The proposed framework progressively narrows down the site selection, balancing computational complexity with model accuracy—from the simple static power flow analysis in the first layout to the eigenvalue analysis with more accurate GFL- and GFM-ESS linear models in the second layout, and finally to the complex time-domain simulations in the third layout. This progression ensures both computational efficiency and enhanced system stability.

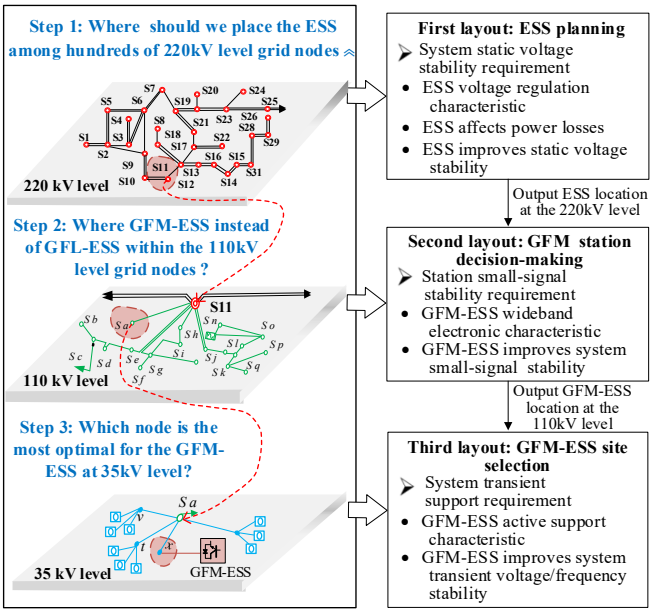

Fig. 1. Proposed framework of the GFM-ESS site selection.

III. Three-Layout GFM-ESS Siting Model

A. GFM control characteristic

The GFM-ESS is equivalent to a controlled voltage source connecting to a low impedance in series, of which detailed configuration and control strategy have been well introduced in the literature, e.g. [29][29]. This model is well-known. Thus, we only briefly introduce its functions and characteristics. Taking the virtual synchronous generation (VSG) as a typical example of the GFM control, the active power control can simulate the power-angle swing equation of SG, thereby providing inertia, damping, and primary frequency regulation to the system, while the reactive power control can regulate the magnitude of the electric potential. Therefore, the GFM-ESS can actively respond to the power system dynamics in terms of the damping and inertia provision, and frequency and voltage support.

In this vein, taking the function of the reactive power compensation of the GFM-ESS can help vary the power flow of the grid and thus improve the static voltage stability in the 220 kV transmission network. The damping effect of the GFM-ESS helps improve the small-signal stability and avoid oscillation at the 220/110 kV collector substation level. The frequency and voltage support capability of the GFM-ESS helps improve the local dynamic voltage and frequency performance of the power system.

The following subsections describe the GFM-ESS planning model for each layout of the proposed hierarchical framework.

B. First layout: ESS planning model

The first layout identifies the transformer station in the 220 kV network where the GFM-ESS should be deployed downstream, with a scenario-based optimal power flow (OPF). The OPF problem can be solved for multiple representative operating scenarios, including seasonal variations in load and renewable generation.

Based on the PV curves with respect to voltage stability analysis, as shown in Fig. 2, the implementation of the GFM-ESS can raise the maximum output power at the saddle node bifurcation (SNB) point and enhance the voltage stability margin.

We utilize a set of indices to represent the effect of the GFM-ESS implementation on the static voltage stability, as follows.

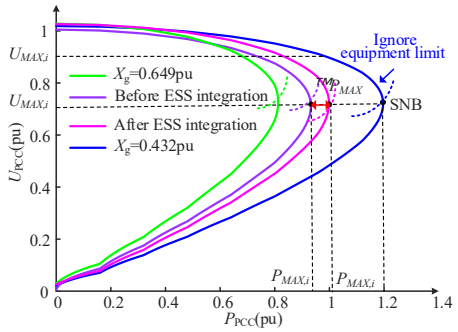

Fig. 2. PV curve before and after the GFM-ESS implementation.

- *Voltage Stability Margin Index* (*VSMI*): This index quantifies the improvement in static voltage stability due to the implementation of GFM-ESS at node *i*.

$$VSMI_i = \frac{VSM_{ess,i} - VSM_{0,i}}{VSM_{0,i}} \quad (1)$$

$$VSM = \frac{U_{MAX} - U_{L0}}{U_{L0}} \quad (2)$$

Where, *VSM* represents the voltage stability margin, and $VSMI_i$ represents the deviation in *VSM* at node *i* before and after the installation of GFM-ESS. U_{MAX} is the voltage value at

the saddle node bifurcation point, and U_{L0} is the voltage value at the current operating point. A larger $VSMI_i$ indicates a better improvement on the voltage stability margin.

- *Voltage Regulation Sensitivity Index (VRSI):* This index quantifies the marginal impact of GFM-ESS implementation at node *i* on the overall static system voltage stability.

$$VRSI_i = \frac{\sum_{m=1}^{n} \left(\frac{U_{mref} - U_m}{U_{mref}}\right)^2}{\sum \Delta U_{base}} \tag{3}$$

Where, U_{mref} is the nominal voltage of node *m*, U_m is the voltage amplitude of node *m*, and $\sum \Delta U_{base}$ is the total offset of the node voltage before the GFM-ESS is implemented. The smaller the value of $VRSI_i$, the higher the sensitivity of node *i* on the voltage regulation.

- *System Loss Index (SLI):* This index captures the impact of GFM-ESS implementation at node *i* on system losses.

$$SLI_i = \sum_{l=1}^{b} R_l I_l^2 \tag{4}$$

Where, R_l is the resistance of branch *l*, I_l is the current of branch *l*. A smaller SLI_i indicates lower system losses.

Considering the characteristics of ESS, one of the optimization objectives of the system is to maximize the static voltage stability margin, and another is to minimize the system losses. Therefore, the first-layout selects *VSMI*, *VRSI*, and *SLI* as siting indices. *VSMI* and *VRSI* represent voltage stability improvements under contingency and normal operation, respectively. *SLI* accounts for system losses, ensuring a balance between stability enhancement and economic efficiency. Based on these indices, the following first layout GFM-ESS siting model is proposed:

$$Min\ f_1(x) = -VSMI \times VRSI \tag{5}$$

$$Min\ f_2(x) = SLI \tag{6}$$

$$J_{ess,k} \in \Upsilon_{see} \tag{7}$$

$$S_{ess,k} \leqslant S_{ess,k}^{max} \tag{8}$$

$$P_{ess,k}^{min} \leqslant P_{ess,k}^{rated} \leqslant P_{ess,k}^{max} \tag{9}$$

$$P_{Gi} - P_{Di} - U_i \sum_{j=1}^{N} U_j \left(G_{ij}\cos\theta_{ij} + B_{ij}\sin\theta_{ij}\right) = 0 \tag{10}$$

$$Q_{Gi} - Q_{Di} + U_i \sum_{j=1}^{N} U_j \left(G_{ij}\sin\theta_{ij} - B_{ij}\cos\theta_{ij}\right) = 0 \tag{11}$$

$$P_{Gi}^{min} \leqslant P_{Gi} \leqslant P_{Gi}^{max} \tag{12}$$

$$Q_{Gi}^{min} \leqslant Q_{Gi} \leqslant Q_{Gi}^{max} \tag{13}$$

$$U_k^{min} \leqslant U_k \leqslant U_k^{max} \tag{14}$$

$$|P_l| = |U_i^2 G_{ij} - U_i U_j \left(G_{ij}\cos\theta_{ij} + B_{ij}\sin\theta_{ij}\right)| \leqslant P_l^{max} \tag{15}$$

Constraints (7)-(9) specify the ESS siting and capacity limits, where $J_{ess,k}$ is the node where GFM-ESS unit *k* is connected, Υ_{see} is the set of potential implementation sites, $S_{ess,k}^{max}$ represents the upper limits of the installed ESS capacity, $P_{ess,k}^{min}$ and $P_{ess,k}^{max}$ represent the lower and upper limits of the ESS power, respectively. Constraints (10) and (11) represent the nodal power balance equality equations. Constraints (12)-(15) specify the limits on the generations and transmission lines. P_{Gi} and Q_{Gi} represent the active and reactive power outputs of generator *i*, respectively; P_{Di} and Q_{Di} represent the active and reactive loads at bus *i*, respectively; U_i and θ_i are the voltage magnitude and phase angle at bus *i*, $\theta_{ij}=\theta_i - \theta_j$; G_{ij} and B_{ij} are the real and imaginary parts of the *i*-th row, *j*-th column element of the bus admittance matrix; and P_l represents the active power flow of line *l*.

C. Second layout: GFM decision model

To identify the optimal 220kV/110kV substation node for small-signal stability of the multi-infeed power electronic system (MIPES) after the implementation of GFM-ESS, this section introduces the gSCR index to assess the small-signal stability of MIPES. The gSCR is defined to quantify the grid strength of the MIPES in terms of its small signal stability.

Based on multi-variable feedback control theory, closed-loop characteristic equation of the MIPES can be decoupled into the MIPES into *n* independent equivalent single-infeed power electronic systems (SIPES) as follows [27].

$$\det\left\{\begin{bmatrix} G_{dd}(s) & G_{dq}(s) \\ G_{qd}(s) & G_{qq}(s) \end{bmatrix} \otimes \boldsymbol{I}_n + \begin{bmatrix} \beta(s) & \alpha(s) \\ -\alpha(s) & \beta(s) \end{bmatrix} \otimes \boldsymbol{S}_B^{-1}\boldsymbol{B}\right\} = 0 \tag{16}$$

In (16), each term is a block diagonal matrix, allowing the characteristic equation of the system to be equivalently transformed into the following form:

$$\prod_{i=1}^{n} \det\left\{\begin{bmatrix} G_{dd}(s) & G_{dq}(s) \\ G_{qd}(s) & G_{qq}(s) \end{bmatrix} + \lambda_i \begin{bmatrix} \beta(s) & \alpha(s) \\ -\alpha(s) & \beta(s) \end{bmatrix}\right\} = 0 \tag{17}$$

Let $\boldsymbol{Y}_{eq} = \boldsymbol{S}_B^{-1}\boldsymbol{B}$, where λ_i represents the *i*th eigenvalue of matrix $\boldsymbol{Y}_{eq}$, and $0<\lambda_1 \leq \lambda_2 \leq \cdots \leq \lambda_n, i = 1, \cdots, n$. Equation (17) states that the characteristic equation of MIPES can be regarded as the product of the characteristic equations of *n* equivalent SIPES, as shown in Fig. 3.

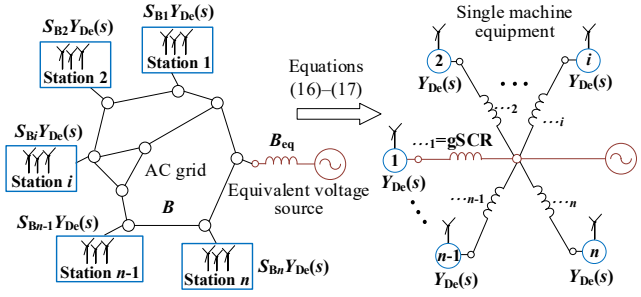

Fig. 3. Schematic diagram of gSCR derivation in MIPES.

The stability of the system, as shown in Fig. 3, depends on the SIPES corresponding to the smallest eigenvalue λ_1 of the matrix $\boldsymbol{Y}_{eq}$. This eigenvalue, λ_1, is defined as the gSCR, which can be used to assess the small-signal stability of MIPES [30].

Installing the GFM-ESS with a capacity of S_{VSG} at node *n* is equivalent to adding a shunt susceptance $S_{VSG}B_p$ to a ground

branch. This modifies the Thevenin equivalent admittance matrix $\boldsymbol{B}$ as follows:

$$\boldsymbol{B}' = \boldsymbol{B} + \begin{bmatrix} 0 & 0 & \cdots & 0 \\ 0 & 0 & \cdots & 0 \\ \vdots & \vdots & & \vdots \\ 0 & 0 & \cdots & S_{\mathrm{VSG}} B_{\mathrm{p}} \end{bmatrix} \tag{18}$$

In this paper, the gSCR is extended to the smallest eigenvalue of the expanded admittance matrix $\boldsymbol{Y}'_{eq}$, accounting for the impact of GFM-ESS.

$$\mathrm{gSCR} = \min\lambda^{+}\left(\boldsymbol{Y}'_{eq}\right) = \min\lambda^{+}(\boldsymbol{S}_{BVSG}^{-1}\boldsymbol{B}') \tag{19}$$

Where $\lambda^{+}(\cdot)$ denotes the positive eigenvalues of the matrix. At this point, all renewable energy converters in the MIPES are operating in discharge mode.

GFL and GFM controls exhibit different output impedance, resulting in different interactions with the grid. It is important to determine whether the ESS should be controlled in GFL or GFM during the planning stage. SCR is an index to represent the strength of the power network and is an affecting factor to the small-signal stability. For the GFL-ESS, the small-signal stability of SIPES degrades along with the SCR decreasing [27]. The critical SCR (CSCR) is defined as the small-signal stability boundary of SIPES with GFL-ESS, in which value the SCR falls below, the system becomes unstable, and the GFM-ESS must be used to sustain the system stability [28]. The SCR is the ratio of the short circuit capacity at the bus to the rated capacity of GFM-ESS.

The CSCR depends on the dynamic characteristics of the GFM-ESS device and is equivalent to the critical value of the single-machine SCR. The value of the CSRC can be obtained through analytical calculations or simulation experiments of a single machine. For multi-infeed systems with homogeneous power electronic devices (PEDs), the CSCR derived from a SIPES can be used to characterize the small-signal stability boundary of MIPES [27]. In our second-layout screening, when evaluating whether an independent GFM-ESS station can be connected to a 35 kV collection station, the rest of the grid is modeled as an infinite bus, effectively simplifying the system to a homogeneous PED configuration. Thus, CSCR serves as a valid criterion for small-signal stability in MIPES.

Additionally, the gSCR is used to evaluate the small-signal stability of the power system implemented with GFM-ESS. The higher the gSCR, the greater the small-signal stability of the system. Therefore, we can use CSCR and gSCR as siting indices to select nodes where GFM-ESS outperforms GFL-ESS. The CSCR provides a stable boundary for the small-signal stability of GFM-ESS, while the gSCR evaluates the small-signal stability of the system after the implementation of GFM-ESS. Thus, we aim to select a site for GFM-ESS installation that maximizes the gSCR, subject to the CSCR constraint. The second layout model is as follows:

$$\begin{cases} \max\ f(x) = \mathrm{gSCR} \\ \text{s.t.}\quad \mathrm{SCR} \le \mathrm{CSCR} \end{cases} \tag{20}$$

D. Third layout: GFM-ESS siting model

A large disturbance in the network causes a nonuniform energy distribution due to factors such as generator inertia, transmission line parameters, and spinning reserves, resulting in varying transient frequency and voltage responses at different nodes. To maximize the GFM-ESS support capability and enhance overall transient stability, this section introduces siting indices to evaluate the effectiveness of GFM-ESS in providing frequency and voltage support.

Figure 4 shows a general profile of the reactive power trajectory during the voltage event, with the critical features marked. These features can be used to evaluate transient voltage stability and dynamic support capabilities. U_{t0} and Q_{t0} are the initial voltage and reactive power values, $\Delta U_{\max}$ is the maximum transient voltage deviation, t_0 is the fault occurrence moment, t_f is the fault clearing moment, and t_c is the voltage recovery moment.

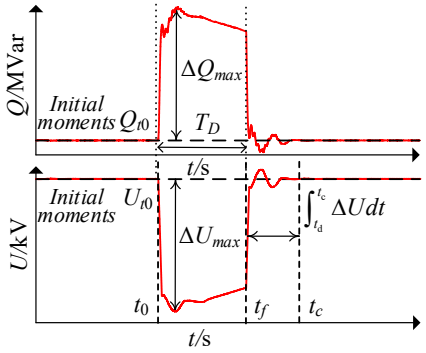

Fig. 4. Reactive power response to voltage variation.

- *Equivalent droop coefficient:* This index is defined as the average reactive power compensation provided by the GFM-ESS at the PCC during fault duration (T_D), reflecting its voltage deviation regulation capability through reactive power-to-voltage control.

$$f_{droop,i}^{F_k} = \frac{\mathrm{avg}_{t_0}^{t_f}|Q_{t,i} - Q_{t0}|}{\mathrm{avg}_{t_0}^{t_f}|U_{t,i} - U_{t0}|} \qquad F_k \in \mathcal{F} \tag{21}$$

Where F_k represents a large-disturbance event, such as generator outage, and short-circuit fault, $\mathcal{F}$ is the anticipated fault set.

In addition, the transient voltage peak $f_{p,i}^{F_k}$ and the degree of transient voltage recovery $f_{r,i}^{F_k}$ are defined as indices for assessing transient voltage stability during large disturbances, as shown in (22) and (23).

$$f_{p,i}^{F_k} = \Delta U_{\max,i} \tag{22}$$

$$f_{r,i}^{F_k} = \int_{f}^{t_c} \frac{|U_{t,i} - U_0|}{U_0} dt \tag{23}$$

Higher values of the indices $f_{p,i}^{F_k}$ and $f_{r,i}^{F_k}$ indicate a higher requirement of voltage support at node i.

By calculating the sensitivity of indices $f_{p,i}^{F_k}$ and $f_{r,i}^{F_k}$, after GFM-ESS implementation, the improvement in transient voltage stability is evaluated, as shown in (24).

$$TVSI_i^{F_k} = x\left|\frac{f_{p-gfm,i}^{F_k} - f_{p-0,i}^{F_k}}{f_{p-0,i}^{F_k}}\right| + y\left|\frac{f_{r-gfm,i}^{F_k} - f_{r-0,i}^{F_k}}{f_{r-0,i}^{F_k}}\right| \quad (24)$$

In (24), "x" and "y" represent the weighting coefficients of two evaluation indices. The larger the $TVSI_i^{F_k}$, the higher the effectiveness of the voltage support in transient.

Fig. 5 shows a general profile of the active power trajectory after the occurrence of the frequency event, highlighting the critical characteristics. P_{t0} and f_{t0} are the initial active power and frequency values, Δf_{max} is the maximum transient frequency deviation, Δf_d is the dynamic frequency difference, RoCoF is the rate of change of frequency, *RoCoP* is the rate of change of power, t_m is the time at the maximum frequency, t_e is the moment of frequency recovery, and t_d is the critical recovery interval following the frequency nadir.

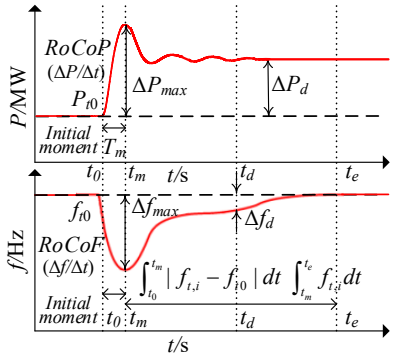

Fig. 5. Active power response to frequency variation.

- *Equivalent inertia index:* This index describes the impact of GFM-ESS power injection at node i on the system RoCoF:

$$g_{RoCoF,i}^{F_k} = \frac{\text{RoCoP}}{\text{RoCoF}} = \frac{\Delta P/\Delta t}{\Delta f/\Delta t} = \frac{P_{t_{m,i}} - P_{t_0}}{f_{t_{m,i}} - f_{t_0}} \quad (25)$$

The higher the value of index $g_{RoCoF,i}^{F_k}$, the stronger the capability of the GFM-ESS inertia response.

- *Equivalent damping index:* This index characterizes the damping effectiveness of the GFM-ESS at node i in suppressing oscillations between the terminal voltage and the internal voltage source:

$$g_{damp,i}^{F_k} = \int_{t_0}^{t_m} |f_{t,i} - f_{t0}|\, dt + \int_{t_m}^{t_e} f_{t,i}\, dt \quad (26)$$

The smaller the value of index $g_{damp,i}^{F_k}$, the greater the capability of the GFM-ESS damping response.

The indices characterizing frequency stability include the rate of change of frequency, transient frequency deviation, and dynamic recovery frequency deviation, as shown in (27)-(29).

$$g_{f,i}^{F_k} = \mathrm{d}f/\mathrm{d}t|_{t=t_0} \quad (27)$$

$$g_{p,i}^{F_k} = \Delta f_{\max,i} \quad (28)$$

$$g_{d,i}^{F_k} = \Delta f_{\mathrm{d},i}|_{t=t_d} \quad (29)$$

The smaller the values of the indices $g_{f,i}^{F_k}$, $g_{p,i}^{F_k}$, and $g_{d,i}^{F_k}$, the higher the benefit from the GFM-ESS installation at the node i on the frequency stability.

The quantitative index of transient frequency stability improvement after GFM-ESS implementation is shown in (30).

$$TFSI_i^{F_k} = a\left|\frac{g_{f-gfm,i}^{F_k} - g_{f-0,i}^{F_k}}{g_{f-0,i}^{F_k}}\right| + b\left|\frac{g_{p-gfm,i}^{F_k} - g_{p-0,i}^{F_k}}{g_{p-0,i}^{F_k}}\right| + c\left|\frac{g_{d-gfm,i}^{F_k} - g_{d-0,i}^{F_k}}{g_{d-0,i}^{F_k}}\right| \quad (30)$$

The larger the $TFSI_i^{F_k}$, the higher the effectiveness of the frequency support in transient. In (30), "a", "b", and "c" represent the weighting factors for GFM-ESS contributions to inertial response, primary frequency regulation and frequency recovery, respectively. Specific values have to be defined based on system support requirements under different grid conditions.

The third layout uses an evaluation model to determine the optimal 110 kV/35 kV substation for GFM-ESS deployment, based on voltage support, frequency support, and transient stability improvement indices.

IV. Proposed Algorithm

The first layout GFM-ESS siting model is used to determine the site at the entire 220 kV network, based on a multi-objective optimization algorithm. The second layout siting targets 110 kV stations connected to the chosen 220 kV/110 kV substations, while the third layout focuses on the specific 110 kV/35 kV substations. The overall flowchart for solving the three-layout optimization model is shown in Fig. 6 with following detailed descriptions.

In the first layout, an optimization algorithm is embedded into the loop of the power flow solver to maximize the voltage stability margin and minimize system losses in the 220 kV network. The system operating condition, including renewable generation and load data, is based on a scenario provided by the TSO. We use DIgSILENT as the power flow solver and the NSGA-II algorithm as the optimization method, as shown in Fig. 6. This is because the NSGA-II algorithm has a high tolerance for the expression of constraints and objective functions in optimization problems.

In the second layout, based on the site selection results, small-signal stability analysis is then used to identify the 220 kV/110 kV substations that present higher gSCR. Here we use the Bode plot to iteratively calculate the CSCR of the GFM-ESS station. Then, we further calculate the gSCR of candidate substations that meet the CSCR constraint.

In the third layout, the scope of the candidate site would be very narrow and because of this, it is possible to run the time-domain simulation of possible scenarios. Here, the Monte

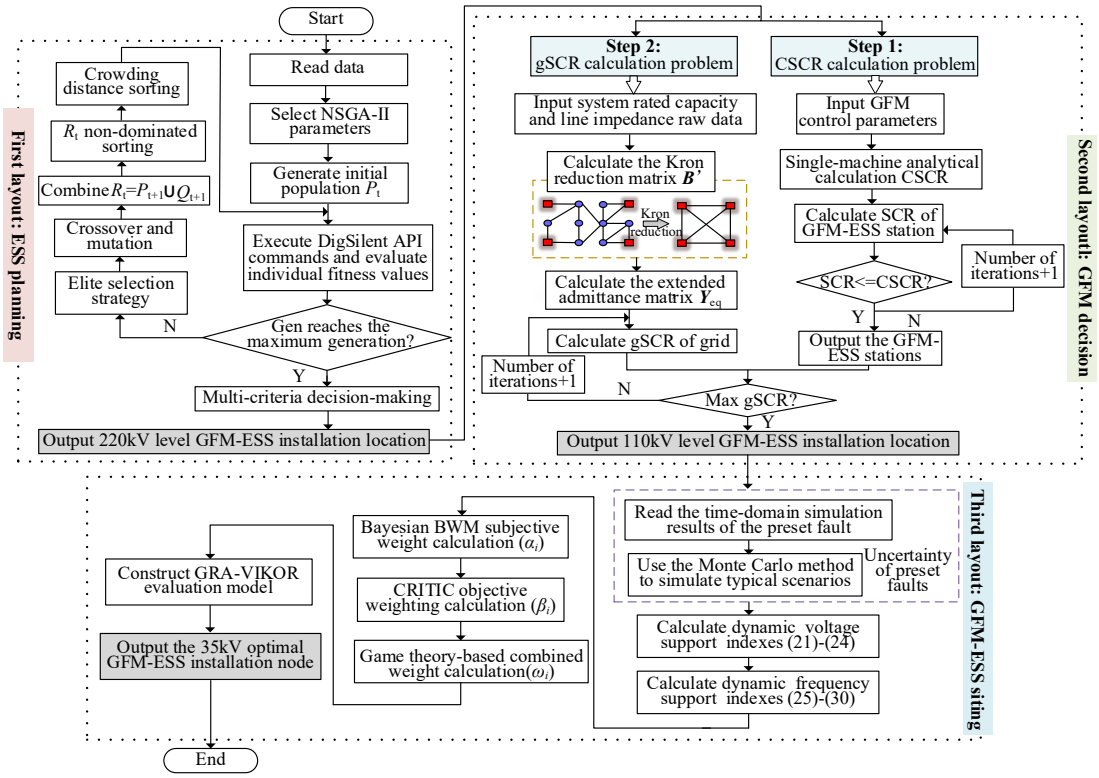

Fig. 6. Flowchart of the three-layout siting algorithm.

Carlo method is first used to simulate the uncertainty of fault occurrences. Because both the voltage and frequency stability are under consideration with 10 proposed indices, in order to balance the positive effects between these two stability types, the weighting calculation method along with the evaluation method is used to ultimately determine the specific optimal site for GFM-ESS installation. We use the Bayesian Best-Worst Method (BWM) for subjective weighting, the CRITIC method for objective weighting, and GRA-VIKOR for evaluation—a hybrid approach that integrates Grey Relational Analysis to handle uncertainty and VIKOR for balanced multi-criteria decision-making. The transition logic among different siting layers is illustrated in Algorithm I.

Algorithm 1: Inter-Layout Transition Logic of Siting Model.

Input: 1.System steady-state data, $\boldsymbol{x}_1^t = \{P_1^t, \cdots, P_n^t; Q_1^t, \cdots, Q_n^t; V_1^t, \cdots, V_n^t; \theta_1^t, \cdots, \theta_n^t; PF_1^t, \cdots, PF_n^t\}$
2. $\boldsymbol{B}$ (Nodal admittance matrix), $\boldsymbol{S}$ (Equivalent device capacity matrix)
3. System transient data under N-1 contingency,
$\boldsymbol{x}_2^t = \{f_1^t, \cdots, f_n^t; P_1^t, \cdots, P_n^t; V_1^t, \cdots, V_n^t; Q_1^t, \cdots, Q_n^t\}$
4. Decision variables, $x_i^{220}, \forall i \in \mathcal{N}_{220}$, $x_j^{110}, \forall j \in \mathcal{N}_{110}$, $x_k^{35}, \forall k \in \mathcal{N}_{35}$
5. Optimization algorithm parameters
Output: Optimal site for GFM-ESS installation
While not all layouts are completed **Do**
Solve first layout model Π_1 over the entire 220 kV network
→ generate candidate set x_i^{220} for second layout (110 kV),
▷ Π_1 = min f_1(x), f_2(x), s.t. (7)-(15)
Solve second layout model Π_2 ← For each bus ∈ Solve (Π_1)
→ generate candidate set x_j^{110} for third layout (35 kV),
▷ Π_2 = max gSCR, s.t. SCR ≤ CSCR
Solve third layout model Π_3← For each bus ∈ Solve (Π_2)
→ output final 35 kV site x_k^{35}
▷Π_3: frequency and voltage stability evaluation model
Return: Final siting obtained from the third layout

V. Real-World Case Study

A large-scale real-world power system in Western China is used as a case study to validate the proposed GFM-ESS site selection strategy. This system has a high renewable penetration of 67.31%, a relatively scattered load, and ±800 kV HVDC transmission to Eastern China, making it highly susceptible to frequency and voltage instability. In such a system, proper GFM-ESS site selection would significantly enhance the stability of the entire regional power system. In the case study, we consider the summer-high-RES scenario, using load and renewable-generation profiles sourced from the TSO. The proposed framework is scenario-agnostic and can incorporate multiple seasonal/operating conditions as well as alternative network configurations.

In this section, we use DIgSILENT software to build the grid model, with its network structure and line parameters shown in Fig. 7. The GFM-ESS model is constructed based on actual data, with control parameters listed in Table I. In our selected regional power system, there are a total of 50 220 kV/110 kV substations. Each 220 kV/110 kV substation is typically connected to 6 to 8 110 kV/35 kV substations. The total the total number of 110 kV/35 kV substations would be above 400 so that it would be time-consuming to try all possible locations and run a stability analysis for each location. Additionally, the grid model includes 70 wind farms and 41 PV power plants, with a total capacity of 11712 MW, and 13 thermal power plants near the HVDC rectifier station with a rated output of 5690 MW. In this case study, the capacity of the planned GFM-ESS station is 100 MW. The overall three-layout siting problem is solved by Python 3.10 interfacing with DIgSILENT 2022 on a host equipped with an Intel(R) Core(TM) i7-12700F CPU @ 2.1

GHz and 32 GB RAM. The total runtime of the three-layout siting process is 5.56 hours. The algorithm settings for the three-layout siting model are given in Table II. For NSGA-II, the search terminates at the maximum generation count (N_{max}=500).

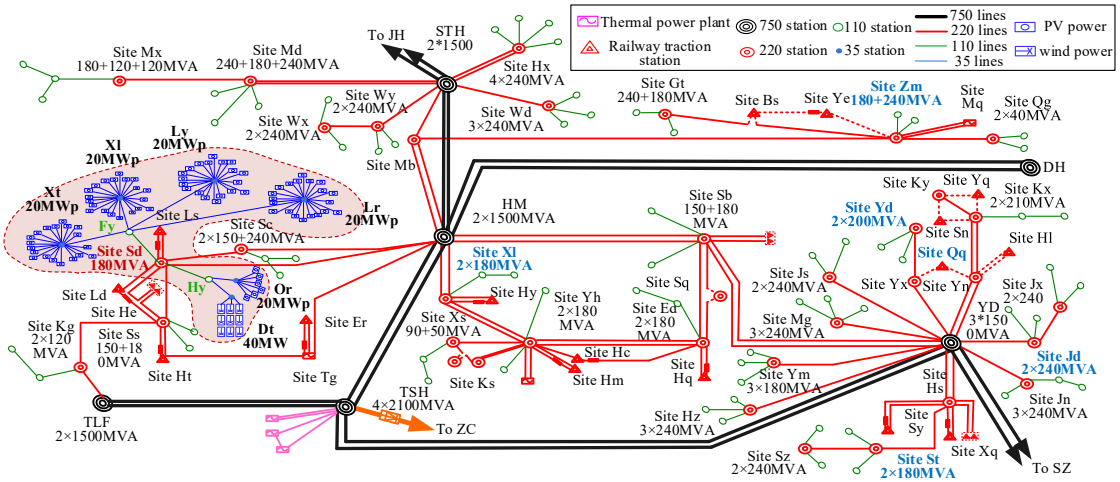

Fig. 7. Structure of the power system in Western China.

TABLE I
GFM-ESS CONTROL PARAMETERS AND NETWORK PARAMETERS

parameter	value	parameter	value	parameter	value
Rated apparent power(S_{ess})	2 MVA	Reactive droop(D_q)	0.5	220 lines-resistance(R_g)	0.0509 Ω/km
Rated power factor	0.9	Filter inductance(L_f)	0.05 p.u.	750 lines-resistance(R_g)	0.0128 Ω/km
Parallel units	50	Filter capacitance(C_f)	0.05 p.u.	110 lines-resistance(R_g)	0.132 Ω/km
Acceleration time constant (T_j)	3 s	Virtual resistance(R_v)	0.006 p.u.	HVDC rated power	4000 MVA
Virtual damping(D_p)	30	Virtual reactance(X_v)	0.006 p.u.	DC rectifier resistance	2 mΩ

TABLE II
ALGORITHM SETTINGS FOR THE THREE-LAYOUT SITING MODEL

Parameter	Value	Parameter	Value
Population size (P_t)	300	GRA coeff. (ρ)	0.50
Offspring size (Q_t)	50	VIKOR coeff. (v)	0.50
Max gens (N_{max})	500	Voltage stability weighting (x,y)	0.50
Crossover rate (p_c)	0.70	Frequency stability weighting (a,b)	0.40
SBX (η_c)	30	Frequency stability weighting (c)	0.20

A. First layout: Static voltage stability requirement

Figure 8 shows the PV curves of the critical bus after individually installing GFM-ESS at each substation within the 220 kV network. For clarity, only a selection of most representative nose-curves is shown in the figure. The results show that the maximum output power varies when implementing GFM-ESS at different substations, indicating that there is an optimal installation location that can maximize the static voltage stability margin.

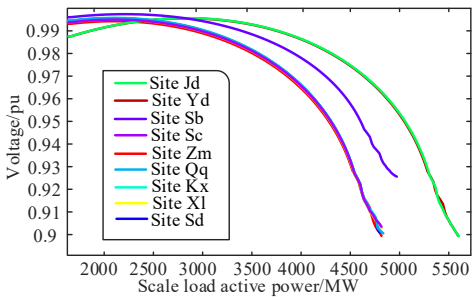

Fig. 8. PV curves for stations after GFM-ESS implementation.

The first layout takes both the static voltage stability margin and the cost of system losses into consideration. Using the NSGA-II multi-objective optimization algorithm, a set of non-dominated GFM-ESS location solutions is obtained. The optimal solution is then chosen by means of the pseudo-weight decision method, as shown in Fig. 9.

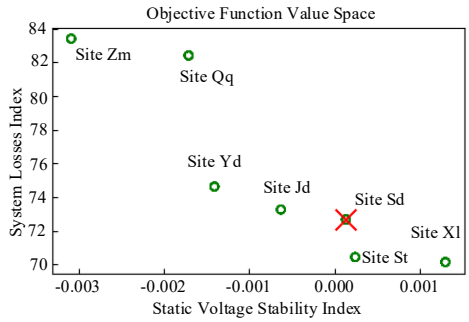

Fig. 9. The optimal solution of the pseudo-weight decision method.

In Fig. 9, the x-axis represents the voltage stability improvement objective function, where a smaller value indicates a greater contribution to static voltage regulation and stability. The y-axis represents the system losses objective function, with a smaller value indicating lower system losses and higher grid efficiency. The optimal solution is determined as Site Sd, which presents good static voltage stability while also having lower line losses. Thus, the siting result for the 220 kV network is Site Sd, which is then input into the second layout.

B. Second layout: Station small signal stability requirement

The second layout is divided into two steps: the first step calculates CSCR, and the second step calculates gSCR.

On the one hand, the CSCR for the single GFM-ESS is calculated. Using the sequence impedance model [31][31], the amplitude-frequency response characteristics of the GFM can be determined. Fig. 10 shows the bode plot of the GFM-ESS under different SCRs. The small-signal stability of the GFM is assessed by the phase margin γ, which is typically set above 30° to ensure a solid stable system. In this case, we adjust the SCR until the phase margin equals 30°, at which point the corresponding SCR is set to be the CSCR. As shown in Fig. 10, when γ = 30°, SCR = 2.03, so that CSCR=2.03.

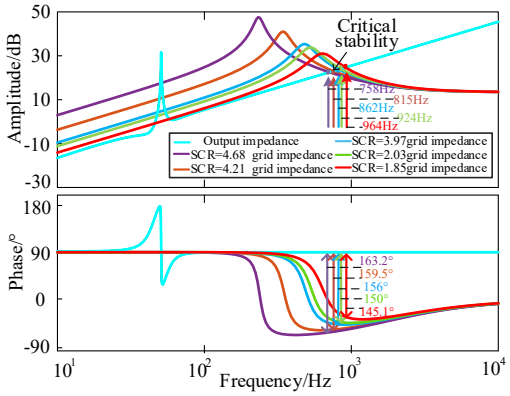

Fig. 10. Bode plot for different SCRs.

As shown in Fig. 7, there are two 220 kV/110 kV substations connected to Site Sd, namely Fy and Hy. The SCR values of the two substations were calculated based on the short-circuit calculation module in DIgSILENT, resulting in 1.99 and 1.98, respectively. Therefore, both Site Fy and Site Hy satisfy the small-signal stability condition required for GFM-ESS installation, i.e., SCR ≤ CSCR. On the other hand, the gSCR of this power system is calculated after the implementation of GFM-ESS at the 220 kV/110 kV substations. Meanwhile, the dominant eigenvalue and damping ratio have also been calculated correspondingly as shown in Table III.

TABLE III
gSCR, dominant roots and damping ratio

Install node	Dominant eigenvalue	Damping ratio	gSCR
Site Fy	-5.000±29.581*i*	0.167	2.431
Site Hy	-4.849±29.144*i*	0.164	1.790

Table III indicates that if GFM-ESS is installed at Site Fy, gSCR = 2.431, while at Site Hy, gSCR = 1.790. The higher gSCR value at Site Fy demonstrates that Site Fy provides superior small-signal stability. From the dominant eigenvalues of Site Fy and Site Hy, it can be seen that Site Fy has a smaller negative real part, indicating a faster decay rate and better stability. Moreover, Site Fy has a larger damping ratio and would contribute to suppressing oscillations. Therefore, the siting result of the second layout is Site Fy.

C. Third layout: System dynamic support requirement

This section uses the Monte Carlo method to randomly generate 500 expected accident scenarios based on the data of possible N-1 contingencies. Table IV shows the Site Ly has the largest $f_{p,i}^{Fk}$, and Site Lr has the largest $f_{r,i}^{Fk}$, suggesting that both sites present poorer transient voltage stability and have a higher demand for voltage support. Meanwhile, Site Lr shows the highest values for $f_{droop,i}^{Fk}$ and $TVSI_i^{Fk}$, with values of 15.255 and 0.473, respectively, indicating that installing the GFM-ESS at Site Lr would provide comparatively stronger voltage support and significantly benefit the transient voltage stability.

TABLE IV
The values of the voltage support index

Index	Station				Combined weight (ω_i)
	Site Xl	Site Ly	Site Lr	Site Xt	
$f_{droop,i}^{Fk}$	7.364	14.071	15.255	13.952	0.1048
$f_{p,i}^{Fk}$	0.0706	0.0707	0.0692	0.0705	0.0590
$f_{r,i}^{Fk}$	0.983	0.969	0.996	0.972	0.0897
$TVSI_i^{Fk}$	0.352	0.415	0.473	0.368	0.1619

Table V presents the frequency support effectiveness indices. In this paper, t_d is set to 0.5 s after the occurrence of the fault. The values of $g_{f,i}^{Fk}$, $g_{p,i}^{Fk}$, and $g_{d,i}^{Fk}$ indicate the improvement on frequency stability, with smaller values suggesting better frequency stability enhancement attributed to the GFM-ESS installation. As shown in Table V, the frequency stability is better when the GFM-ESS is installed at Site Lr and Site Xt. Additionally, the values of the $g_{RoCoF,i}^{Fk}$ and $g_{damp,i}^{Fk}$ indicate that the installation of the GFM-ESS at Site Ly provides the best inertial support, while the installation at Site Lr demonstrates the most effective damping support. Furthermore, the transient frequency stability improvement index, $TFSI_i^{Fk}$, shows that the GFM-ESS installation at Site Lr offers the best transient frequency support effectiveness.

TABLE V
The values of the frequency support index

Index	Station				Combined weight (ω_i)
	Site Xl	Site Ly	Site Lr	Site Xt	
$g_{RoCoF,i}^{Fk}$	9.437	13.833	10.682	11.056	0.0775
$g_{damp,i}^{Fk}$	0.101	0.139	0.002	0.143	0.1147
$g_{f,i}^{Fk}$	0.0035	0.003	0.002	0.0035	0.0916
$g_{p,i}^{Fk}$	0.0008	0.0010	0.0006	0.0011	0.0779
$g_{d,i}^{Fk}$	0.9996	0.9995	0.9995	0.9994	0.0482
$TFSI_i^{Fk}$	0.499	0.466	0.667	0.399	0.1748

To systematically evaluate the dynamic support effect of each station, a multi-criteria decision-making approach was adopted. Five experts have been consulted to identify the most and least effective indicators from the siting index system, denoted as A_B and A_W, respectively. Using a 1-9 scale, these indices are compared to construct best-worst comparison matrices. The matrices were then input into the Bayesian BWM model to derive subjective weights, while objective weights are

calculated using the CRITIC method. The consistency precision parameter β_1 had a *posterior* mean of 369.31 (95% CrI: [157.18, 721.69]), indicating high agreement among experts. The subjective and objective weights were integrated using a game theory-based approach to obtain the combined weights ω_i (Tables IV and V), which were applied in a weighted evaluation matrix for the improved GRA-VIKOR model to rank the candidate sites. Relevant parameters are shown in Table VI, where Site Lr has the smallest comprehensive evaluation coefficient T_i, making it the best choice, followed by Site Ly, with Site Xt ranking the lowest. This indicates that Site Lr is the optimal site to implement the GFM-ESS from a power system support perspective.

TABLE VI
Comprehensive siting ranking

Station	GRA-VIKOR			
	Group utility value	Individual regret value	T_i values	Ranking
Site Xl	5.6232	0.1619	0.9269	3
Site Ly	4.9222	0.1311	0.7175	2
Site Lr	1.1987	0.0590	0	1
Site Xt	5.7827	0.1748	1.0000	4

D. Comparative Analysis of Multiple Scenarios

The hierarchical site selection strategy proposed in this paper optimizes the placement of GFM-ESS with respect to the power system stability enhancement in multi-scales. To validate the effectiveness of the hierarchical site selection method for GFM-ESS optimization, three scenarios with varying levels of selection indices were set up for comparison.

- Scenario 1: considers only first layout indices.
- Scenario 2: includes first and second layouts.
- Scenario 3: applies the proposed three-layout model.

The site selection results for Scenario 1, Scenario 2, and Scenario 3 are Site Or, Site Xt, and Site Lr, respectively. Fig. 11 presents the stability enhancement effects for these three scenarios. The *y*-axis is the coefficient that represents the improvement in stability, the larger the value, the better the stability enhancement. The *x*-axis represents the sites corresponding to the three scenarios. The T_i value is the comprehensive evaluation coefficient, where a smaller value indicates a higher ranking.

As shown in Fig. 11, Site Or focuses exclusively on optimizing static voltage stability, leading to deficiencies in small-signal and transient stability. Site Xt has achieved significant improvements in both static voltage stability and small-signal stability. Site Lr incorporates optimizations across static voltage stability, small-signal stability, and transient stability, achieving superior and balanced effects. The value T_i calculated by the GRA-VIKOR method indicates that Site Lr with the smallest T_i value is the optimal choice. This further validates the effectiveness and superiority of the multi-layout site selection strategy.

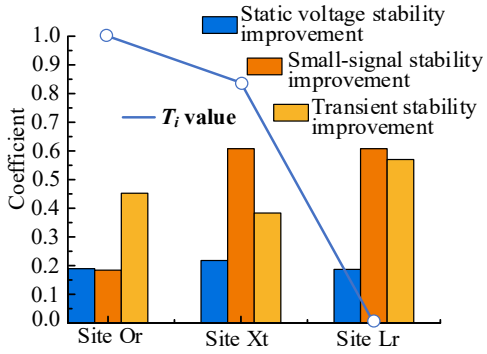

Fig. 11. Comparison of the effect of GFM-ESS siting in different scenarios.

Figures 12 shows the frequency and RoCoF at the upstream collector substation after the system is subjected to the HM-STH 750 kV open circuit contingency, with GFM-ESS installed at each of the three sites. Site Xt presents the highest peak in frequency deviation after the initial disturbance and prolonged RoCoF oscillations, indicating poor frequency stability. Although the peak frequency deviation at Site Or is slightly lower than that at Site Xt, it undergoes the largest RoCoF variation. In contrast, Site Lr demonstrates the most stable performance in terms of both frequency deviation and RoCoF, with rapid recovery and minimal transient deviation. The results in Fig. 12 show that installing GFM-ESS at Site Lr achieves the best frequency support capability, which reduces the maximum frequency deviation and RoCoF by 45.45% and 42.86%, respectively, compared to the system without GFM-ESS.

Fig. 13 shows the result of the voltage deviation for each site in the time-domain simulation after the system is subjected to the HM-STH 750 kV line three-phase short circuit contingency. In terms of peak voltage deviation and recovery speed, Site Lr consistently demonstrates a better transient response than the other two sites. Installing GFM-ESS at Site Lr reduces the maximum voltage deviation by 67.91% compared to the system without it. This comparative study reveals that the installation of the same GFM-ESS at Site Lr outperforms that at other sites in both voltage and frequency support, achieving the most significant improvement in voltage and frequency stability.

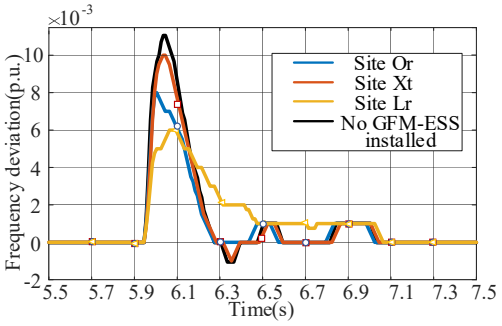

(a) Frequency deviation

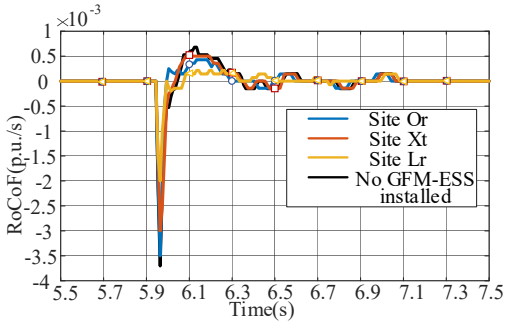

(b) RoCoF

Fig. 12. Results in time-domain simulation.

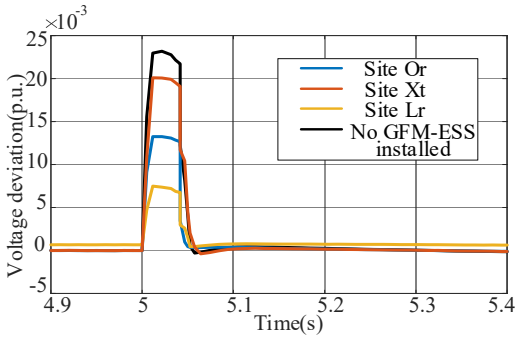

Fig. 13. Result of the voltage deviation in time-domain simulation.

E. Comparative analysis with full-network evaluation

To verify the effectiveness of the proposed hierarchical siting strategy in comparison with a full-network evaluation, we exhaustively enumerate the installation of the GFM-ESS at each 35 kV substations in the network and compare the system performance following open-circuit and short-circuit contingencies. Figures 14 and 15 show frequency and voltage deviations at the upstream 220 kV substation after installing GFM-ESS at its 35 kV substations, where the red curves represent the selected optimal site, the blue curves represent the first-layout Pareto-optimal set, and the gray curves represent the remaining candidate sites.

Results in Fig. 14 show that most substations (represented by gray curves) exhibit large frequency deviations around 0.004 p.u. and slow recovery, while the first-layout Pareto set shows smaller deviations and faster stabilization. The selected optimal site achieves relatively favorable performance with smaller transient deviation and faster stabilization.

Results in Fig. 15 shows that the substations represented by the gray curves exhibit a clear voltage drop of about 0.12 p.u., followed by slow recovery, whereas the first-layout Pareto set shows improved voltage transients. The optimal site again shows relatively better voltage response, maintaining deviations within a narrow range and recovering faster. In summary, the first-layout Pareto set already covers nodes with superior dynamic characteristics, and the final optimal site achieves the best overall performance across static, small-disturbance and transient stability. Furthermore, compared with the exhaustive full-network evaluation that required 123.46 h, the proposed strategy required only 5.56 h, reducing computation time by 95.5% while still maintaining robust and representative results.

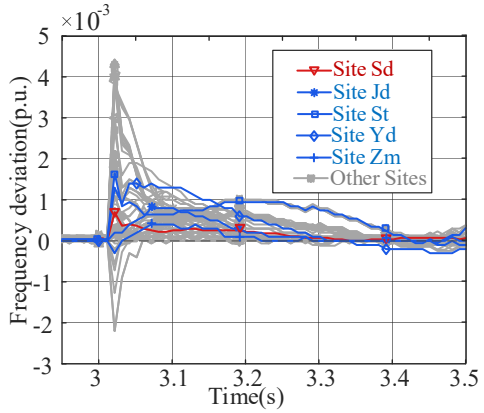

Fig. 14. Frequency deviation at all 220 kV substations with GFM-ESS.

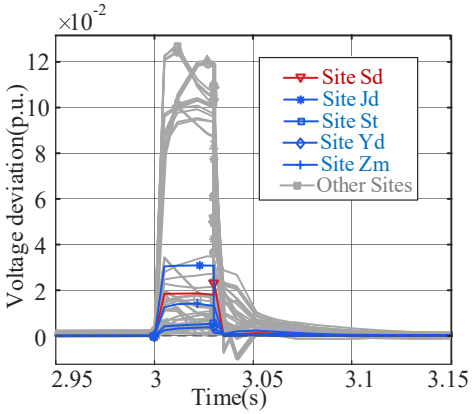

Fig. 15. Voltage deviation at all 220 kV substations with GFM-ESS.

VI. Conclusions

This paper proposes a hierarchical site selection optimization method to improve the multi-timescale stability of high-renewable-energy power systems. The effectiveness of this strategy is validated through a case study of the actual power system in Western China. The main conclusions of this work are as follows:

(1) The proposed siting strategy can effectively enhance the voltage stability of the system while considering economic efficiency, ensuring the small-signal stability of GFM station, and maximizing the support capacity of the device.

(2) The proposed hierarchical method effectively narrows the selection range from the entire system at the beginning to a specific 110 kV/35 kV site at the end, significantly streamlining the siting process and reducing computational complexity.

(3) The proposed method was validated through time-domain simulations. The results prove that the three-layout siting strategy optimizes the entire system stability under the implementation of the same capacity of the GFM-ESS.

In future work, we will test alternative algorithms for each stage of the proposed hierarchical framework to verify its effectiveness. Additionally, we will further explore transforming multi-scale stability indices into constraints for direct integration into the optimization function, enabling efficient solving through convexification techniques.

VII. References

[1] F. Milano, F. Dörfler, G. Hug, D. J. Hill and G. Verbič, "Foundations and Challenges of Low-Inertia Systems (Invited Paper)," in *2018 Power Systems Computation Conference (PSCC)*, Dublin, Ireland, 2018, pp. 1-25.

[2] Z. Tang, Y. Yang and F. Blaabjerg, "Power electronics: The enabling technology for renewable energy integration, " *CSEE Journal of Power and Energy Systems*, vol. 8, no. 1, pp. 39-52, Jan. 2022.

[3] Y. Gu and T. C. Green, "Power System Stability with a High Penetration of Inverter-Based Resources," in *Proceedings of the IEEE*, vol. 111, no. 7, pp. 832-853, Jul. 2023.

[4] J. Chen, M. Liu, F. Milano, et al, "100% Converter-Interfaced generation using virtual synchronous generator control: A case study based on the irish system," *Electric Power Systems Research*, vol. 187, pp. 106475, Oct. 2020.

[5] X. Wu, S. Wu, F. Wang, et al., "Grid-Forming Control and Experimental Validation for High Voltage Transformerless Battery Energy Storage System," *IEEE Transactions on Power Electronics*, vol. 40, no. 4, pp. 4889-4901, Apr. 2025.

[6] B. Badrzadeh, C. Cardozo, M. Hishida, et al., "Grid-Forming Inverters: Project Demonstrations and Pilots," *IEEE Power and Energy Magazine*, vol. 22, no. 2, pp. 66-77, Mar-Apr. 2024.

[7] J. Chen, M. Liu, F. Milano, and T. O'Donnell, "Adaptive Virtual Synchronous Generator Considering Converter and Storage Capacity Limits," *CSEE Journal of Power and Energy Systems*, vol. 8, no. 2, pp. 580-590, Mar. 2022.

[8] Y. Du, C. Zheng and H. Sun, "Transient stability analysis of multiple GFM converters connected into an equivalent grid from the perspective of unbalanced energy," *CSEE Journal of Power and Energy Systems*, early access, doi: 10.17775/CSEEJPES.2023.08340.

[9] X. Fu, J. Sun, M. Huang, et al., "Large-Signal Stability of Grid-Forming and Grid-Following Controls in Voltage Source Converter: A Comparative Study," *IEEE Transactions on Power Electronics*, vol. 36, no. 7, pp. 7832-7840, Jul. 2021.

[10] H. Zhang, W. Xiang, W. Lin, and J. Wen, "Grid Forming Converters in Renewable Energy Sources Dominated Power Grid: Control Strategy, Stability, Application, and Challenges," *Journal of Modern Power Systems and Clean Energy*, vol. 9, no. 6, pp. 1239-1256, Nov. 2021.

[11] Y. Liu, J. Chen, C. Ge, K. Wang, X. Chang, and Q. Zhao, "Index System for Evaluating the Supporting Capability of the Inverter-based Resource," in *2023 IEEE Power & Energy Society General Meeting (PESGM)*, Orlando, FL, USA, 2023.

[12] Z. Zhou, W. Wang, T. Lan, and G-M. Huang, "Dynamic Performance Evaluation of Grid-Following and Grid-Forming Inverters for Frequency Support in Low Inertia Transmission Grids," in *2021 IEEE PES Innovative Smart Grid Technologies Europe (ISGT Europe)*, 2021.

[13] Y. Sun, Z. Zhao, M. Yang, D. Jia, W. Pei, and B. Xu, "Overview of energy storage in renewable energy power fluctuation mitigation," *CSEE Journal of Power and Energy Systems*, vol. 6, no. 1, pp. 160-173, Mar. 2020.

[14] J. Chen, M. Liu, T. O'Donnell, and F. Milano, "On the Synchronization Stability of Converters connected to Weak Resistive Grids," in *2021 IEEE Power & Energy Society General Meeting (PESGM)*, Washington, DC, USA, 2021, pp. 1-5.

[15] C. Li, Y. Yang, Y. Cao, L. Wang, and F. Blaabjerg, "Frequency and Voltage Stability Analysis of Grid-Forming Virtual Synchronous Generator Attached to Weak Grid," *IEEE Journal of Emerging and Selected Topics in Power Electronics*, vol. 10, no. 3, pp. 2662-2671, Jun. 2022.

[16] R. Rosso, X. Wang, M. Liserre, X. Lu, and S. Engelken, "Grid-Forming Converters: Control Approaches, Grid-Synchronization, and Future Trends—A Review," *IEEE Open Journal of Industry Applications*, vol. 2, pp. 93-109, Apr. 2021.

[17] L. Fiorini, G. A. Pagani, P. Pelacchi et al., "Sizing and siting of large scale batteries in transmission grids to optimize the use of renewables," *IEEE Journal on Emerging and Selected Topics in Circuits and Systems*, vol. 7, no. 2, pp. 285-294, Jun. 2017.

[18] J. Zhang, N. Zhang, and Y. Ge, "Energy Storage Placements for Renewable Energy Fluctuations: A Practical Study," *IEEE Transactions on Power Systems*, vol. 38, no. 5, pp. 4916-4927, Sep. 2023.

[19] R. Minguez, F. Milano, R. Zarate-Minano and A. J. Conejo, "Optimal Network Placement of SVC Devices," *IEEE Transactions on Power Systems*, vol. 22, no. 4, pp. 1851-1860, Nov. 2007.

[20] M-E. Hassanzadeh, M. Nayeripour, S. Hasanvand, et al, "Hierarchical optimal allocation of BESS using APT-FPSO based on stochastic programming model considering voltage sensitivity and eigenvalues analyses," *International Journal of Electrical Power & Energy Systems*, vol. 153, pp. 109291, Nov. 2023.

[21] Y. Cao, Q. Wu, H. Zhang, et al., "Multi-objective optimal siting and sizing of BESS considering transient frequency deviation and post-disturbance line overload," *International Journal of Electrical Power & Energy Systems*, vol. 144, pp. 108575, Jan. 2023.

[22] C. Xu, D. Zhao, X. Feng, R. Tao, and C. Liu, "Multi-damping frequency-constrained unit commitment and multi-reserve resource allocation for RES-penetrated power systems," *CSEE Journal of Power and Energy Systems*, early access, doi: 10.17775/CSEEJPES.2024.02590.

[23] T. Zhao, N. Raghunathan, A. Yogarathnam, et al, "A scalable planning framework of energy storage systems under frequency dynamics constraints," in *International Journal of Electrical Power & Energy Systems*, vol. 145, pp. 108693, Feb. 2023.

[24] C. Yang, L. Huang, H. Xin, and P. Ju, "Placing Grid-Forming Converters to Enhance Small Signal Stability of PLL-Integrated Power Systems," *IEEE Transactions on Power Systems*, vol. 36, no. 4, pp. 3563-3573, Jul. 2021.

[25] Y. Liu, Y. Chen, H. Xin, et al., "System Strength Constrained Grid-Forming Energy Storage Planning in Renewable Power Systems," *IEEE Transactions on Sustainable Energy*, vol. 16, no. 2, pp. 981-994, Apr. 2025.

[26] Z. Chu and F. Teng, "Coordinated Planning for Stability Enhancement in High IBR-Penetrated Systems," *IEEE Transactions on Sustainable Energy*, vol. 16, no. 1, pp. 700-715, Jan. 2025.

[27] W. Dong, H. Xin, D. Wu and L. Huang, "Small Signal Stability Analysis of Multi-Infeed Power Electronic Systems Based on Grid Strength Assessment," *IEEE Transactions on Power Systems*, vol. 34, no. 2, pp. 1393-1403, Mar. 2019.

[28] H. Xin, C. Liu, X. Chen, Y. Wang, E. Prieto-Araujo and L. Huang, "How Many Grid-Forming Converters Do We Need? A Perspective From Small Signal Stability and Power Grid Strength," *IEEE Transactions on Power Systems*, vol. 40, no. 1, pp. 623-635, Jan. 2025.

[29] M. Zhao, X. Yuan, and J. Hu, "Modeling of DFIG Wind Turbine Based on Internal Voltage Motion Equation in Power Systems Phase-Amplitude Dynamics Analysis," *IEEE Transactions on Power Systems*, vol. 33, no. 2, pp. 1484-1495, Mar. 2018.

[30] Y. Liu, X. Lai, H. Xin, J. Zhu, L. Huang and S. Xia, "Generalized Short-Circuit Ratio Based Distributed Real-Time Stability Assessment of Renewable Power Systems," *IEEE Transactions on Power Systems*, vol. 38, no. 6, pp. 5953-5956, Nov. 2023.

[31] G. Li, Y. Chen, A. Luo, et al., "Analysis and Mitigation of Subsynchronous Resonance in Series-Compensated Grid-Connected System Controlled by a Virtual Synchronous Generator," *IEEE Transactions on Power Electronics*, vol. 35, no. 10, pp. 11096-11107, Oct. 2020.